nature materials

Article

https://doi.org/10.1038/s41563-025-02384-7

High-performance graphene-based carbon fibres prepared at room temperature via domain folding

Received: 14 October 2024

Accepted: 22 September 2025

Published online: 20 October 2025

Check for updates

Peng Li[1,3], Ziqiu Wang[1,3], Gangfeng Cai[1,3], Yingjie Zhao[2], Zihao Deng[1], Bo Wang[1], Zheng Li[1], Xin Ming[1], Weiwei Gao[1], Zhen Xu[1] ✉, Zhiping Xu[2] ✉, Yingjun Liu[1] ✉ & Chao Gao[1] ✉

The assembly of strong graphene into high-performance macroscopic materials has attracted great interest and sustained attention. Thermal treatment has proven effective in improving the performance by restoring pristine graphene lattice from defective graphene oxide. However, the mechanical performance of graphene fibres remains inferior to that of single-layer pristine graphene, primarily due to assembly-induced defects such as microvoids that form during the folding process of two-dimensional sheets to fibre structures. Here we report the room-temperature fabrication of ultrastrong and stiff graphene fibres, which exhibit an average tensile strength of 5.19 GPa and Young's modulus of 529 GPa. We propose a domain-folding strategy to construct highly folded yet densely packed nanotexture, resulting in a tenfold reduction in microvoid volume. The stress distribution within the fibres is homogenized, leading to enhanced mechanical properties. These findings advance the fabrication of carbon fibres and other macroscopic materials assembled from two-dimensional nanosheets, enabling high material quality with reduced energy consumption.

Carbon fibre (CF), well known for its excellent specific strength and stability[1], boosted the development of airplane and spacecraft, and has been extended to vehicles, wind turbine blades and energy batteries[2–5]. These properties originate from its pure carbon component, which is composed of ordered graphene-based sp^2 structures[6]. Since its invention, the formation of graphene units in CFs has always relied on an organic carbonization method, in which linear polymer or small organic molecules are fused into graphene units under a sufficiently high temperature, usually above 1,300 °C (refs. 7,8). Only then does the fibre obtain a high carbon content over 90%. As a result, the conventional organic carbonization path comes with massive energy consumption, 17 times as that in the case of steel[9]. This high-temperature treatment accounts for about 40% of the total cost[10]. There is a long-standing challenge of the low-temperature production of CFs and cutting down energy consumption. However, the conventional carbonization principle makes it impossible to substantially lower the processing temperature and maintain high performance. Considering that all the outstanding performances originate from graphene-based sp^2 carbon units, beyond the carbonization protocol, we wonder that directly fabricating CFs from the structural unit of graphene should

[1]MOE Key Laboratory of Macromolecular Synthesis and Functionalization, Zhejiang Key Laboratory of Advanced Organic Materials and Technologies, International Research Center for X Polymers, Research Center for Advanced Fibers, Department of Polymer Science and Engineering, Zhejiang University, Hangzhou, China. [2]Applied Mechanics Laboratory, Department of Engineering Mechanics and Centre for Nano and Micro Mechanics, Tsinghua University, Beijing, China. [3]These authors contributed equally: Peng Li, Ziqiu Wang, Gangfeng Cai. ✉e-mail: zhenxu@zju.edu.cn; xuzp@tsinghua.edu.cn; yingjunliu@zju.edu.cn; chaogao@zju.edu.cn

https://doi.org/10.1038/s41563-025-02384-7

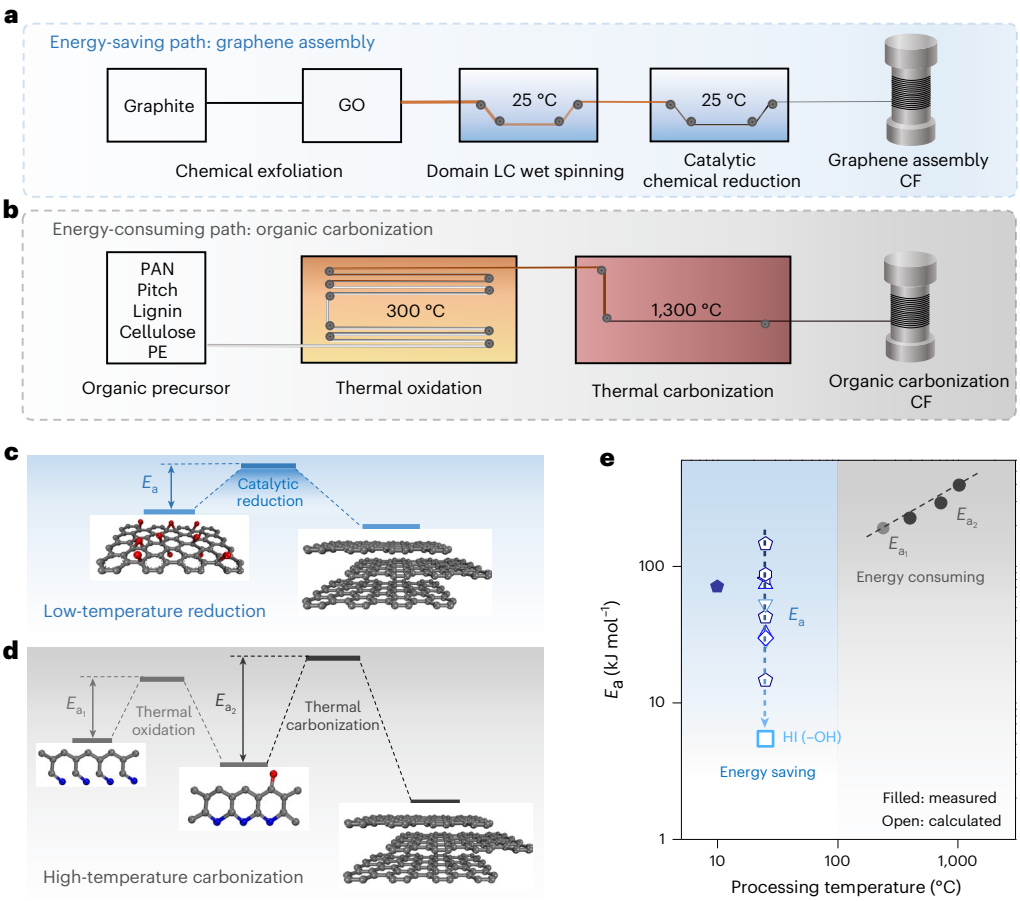

Fig. 1 | Contrast of two paths towards CFs. a, Schematic of the energy-saving path of GF preparation at room temperature, with simple steps involving the chemical exfoliation of natural graphite, domain LC wet spinning and catalytic chemical reduction. **b**, Schematic of traditional CF preparation at a high temperature of 1,300 °C, with energy-intensive steps involving thermal oxidation and thermal carbonization. **c**,**d**, Schematic of room-temperature reduction of GO (**c**) and high-temperature carbonization of organic PAN (**d**). **e**, E_a versus processing temperature in GO chemical reduction of different agents and PAN carbonization.

achieve the preparation of CFs at low temperature, potentially even at room temperature.

Graphene fibres (GFs) were initially fabricated via the wet spinning of graphene oxide (GO) liquid crystals followed by chemical reduction (with a tensile strength of 140 MPa) in 2011 (ref. 11). Improvement in the mechanical properties of GFs was achieved by aligning graphene sheets and enlarging graphitic crystallites following the same high-temperature treatment with conventional CFs. A tensile strength of 1.08 GPa was obtained for crystalline GFs fabricated by mixing large- and small-sized GO sheets following annealing treatment at 1,800 °C (ref. 12). Narrowing the spinning microchannel (enhancing the shear stress) and post-plastic stretching improved the alignment of GO sheets along the fibre axis, leading to a highly crystalline graphitic structure and improved tensile strength to 1.9–3.4 GPa after thermal annealing above 2,500 °C (refs. 13–15).

Although pristine graphene lattice and crystalline structures are well restored in high-temperature treatment, the defects forming in the macro-assembly process still heavily limit the mechanical properties of GFs. Specially, since the GO spinning dope is normally dilute (around 1–2 wt%) for its high excluded volume, GO gel fibre would shrink severely by collapsing GO sheets (50–100 times) to form a solid fibre during wet spinning[16], resulting in these assembly defects such as microvoids and wrinkles. Generally, enhancing the stress transfer among molecules, such as improving the alignment, removing microvoids and increasing interlayer interaction leads to improved tensile properties, carbon nanotube fibres and GFs[1,4,13,15,17,18]. Minimizing this defect forming in the macro-assembly process promises to enhance the stress transfer and to obtain high-performance graphene-based CFs even prepared under room temperature.

Here we report a high-performance graphene-based CF prepared at room temperature through a domain-folding strategy to minimize assembly defects, which is different from the conventional organic carbonization path (Fig. 1a,b). Beyond previously reported GFs[15,19,20], GF prepared at room temperature exhibits a breakthrough in mechanical properties with a high average strength of 5.19 GPa and high Young's modulus of 529 GPa. Simultaneously, the graphene assembly path has a merit in the functional performance of CFs. The GF exhibits an excellent thermal conductivity of 232 W m^{-1} K^{-1}, far exceeding that (below 32 W m^{-1} K^{-1}) of high-strength polyacrylonitrile (PAN) CFs by 625%.

Room-temperature graphene assembly path

The graphene assembly path involves three major steps: chemical exfoliation of graphite to obtain GO, domain LC wet spinning and catalytic chemical reduction (Fig. 1a). Commercially accessible GO was controllably produced in tonnes and used for wet spinning. In domain LC wet spinning, a microgrid with a given size of square holes (size of D^2) was introduced into the spinneret to separate the fluid into finer streamlets; then, finer domains fused in situ and domain folded into a single solid fibre (Supplementary Fig. 1)[21,22]. Solvation drawing was used to fully align the solid graphene oxide fibre (GOF). Finally, GOF was catalytically

reduced by hydroiodic acid accompanied with trifluoroacetic acid to continuously get GF at room temperature. These three steps were carried out at room temperature and the whole processing of GF is a wet method, similar to the production of usual synthetic fibres, such as vinylon and acrylic fibres for clothes. By contrast, the production of traditional CFs is stepwise processed through thermal oxidation at around 300 °C and carbonization above 1,300 °C (Fig. 1b).

In the principle of reaction kinetics, the assembly path of graphene sheets greatly lowers the processing temperature compared with the traditional organic carbonization path. The reaction temperature should be sufficiently high to overcome the kinetic activation energy (E_a) and the reaction rate coefficient (k) is determined as $k = Ae^{-\frac{E_a}{RT}}$, where A is the pre-exponential factor for the reaction, R is the universal gas constant and T is the absolute temperature[23]. Efficient catalytic reduction using hydroiodic acid and trifluoroacetic acid ensures the room-temperature preparation of GFs. Density functional theory calculations using intrinsic reaction coordinates demonstrated that the value of E_a in catalytic reduction by hydroiodic acid is small down to 5.4 kJ mol^{-1} for hydroxyl groups and 36.0 kJ mol^{-1} for epoxy groups, respectively (Fig. 1c–e and Supplementary Fig. 2), which are much lower than thermal reduction (130 to 170 kJ mol^{-1}; Supplementary Table 1). For the formation of graphitic carbon, the path of assembling graphene sheets only needs to eliminate functional groups decorated on the backbone of graphene (Fig. 1c). On the contrary, in the path of organic carbonization, small or linear molecules are gradually fused into graphene backbones through condensation and crystallization (Fig. 1d). The selection of the reaction path enables the preparation of graphitic carbon materials at low temperature. The room-temperature preparation of GF gets rid of the indispensable high-temperature condition and cuts down the energy cost by about 97% of traditional CFs (Fig. 1e, Supplementary Fig. 3 and Supplementary Table 2), exhibiting superiority in saving energy.

Domain folding of graphene sheets

The domain folding of individual GO sheets contributes to the strengthening of GF in our graphene assembly path. In the domain LC wet spinning, a meta-liquid crystal texture was observed, which was composed of a bundle of identically finer domains (Fig. 2a and Supplementary Figs. 1 and 4). Due to the much smaller domain size, GO sheets (average lateral size, 101 μm; Supplementary Fig. 5) are highly folded in each fine domain and the subsequent coagulation and solidification processes further accelerate the severe folding of GO sheets with the kept relative positions (Supplementary Fig. 6), thereby called domain folding. Inspired by multiscale hierarchical structures of natural muscle and wood[24], domain folding yields hierarchically interfused fibrils with a radial, highly folded structure within a solid domain-folded GOF, accompanied with small interlocked assembled graphene folds and minimized microvoids among small folds (Fig. 2b,c and Supplementary Figs. 7 and 8a). Meanwhile, wrinkles were further flattened by solvation drawing to align the GO sheets along the fibre axis[15]. After room-temperature chemical reduction, GFs with a highly folded structure were continuously collected (Supplementary Fig. 9). A control fibre without domain folding was also prepared. In this process, two-dimensional graphene sheets are randomly and freely folded into a fibre, yielding a highly extended structure with large assembled graphene folds and large microvoids (Fig. 2d,e and Supplementary Fig. 8b). For clarity, domain-folded and free-folded GFs/GOFs are labelled as df-GFs/GOFs and ff-GFs/GOFs, respectively.

The highly folded structure in the cross-section of df-GF represents an innovative model of GF, different from that in conventional ff-GF (highly extended). According to the Griffith's fracture theory[25], tensile strength $\sigma = \sqrt{\frac{2E\gamma}{\pi a}}$, where E is the elastic modulus, γ is the specific surface energy and a is half of the crack length, and minimizing the defect size would reduce the stress concentration and improve the tensile strength of fibres. The microvoid content primarily influences the load transfer and, thus, the mechanical properties by decreasing the load-bearing volume[26]. Uniformly distributed microvoids are also helpful for fibre strengthening. We constructed three-dimensional (3D) fibre structures by focused-ion-beam (FIB) and scanning electron microscopy (SEM) tomography to exactly demonstrate the dramatic differences in microvoid defects between ff-GF and df-GF. The df-GF exhibits a much lower porosity compared with ff-GF (Fig. 2f,g and Supplementary Fig. 10). The volume distributions of 3D-reconstructed microvoids show an order of magnitude decrease for df-GF compared with ff-GF (Fig. 2h,i). Since graphene sheets are highly folded by domain folding, the df-GF only shows less and evenly distributed microvoids. On the contrary, much more microvoids were clearly observed in the ff-GF, even overlapping in the transparent 3D view.

Typical microvoids with median volume in df-GF and ff-GF intuitively show the differences of size and shape. The median microvoids show spatial sizes of 214 nm × 75 nm × 40 nm in ff-GF and 168 nm × 18 nm × 21 nm in df-GF, respectively. The volume of median microvoids in ff-GF (2.09×10^{-4} μm^3) is more than ten times that of df-GF (1.79×10^{-5} μm^3). Additionally, the typical microvoid of ff-GF has a planar cross-section, which comes from the stacking gaps among large assembled graphene folds. On the contrary, the cross-section of the typical microvoid in df-GF is acicular owing to the dense stacking of smaller assembled graphene folds. Molecular dynamics simulations were conducted to visually depict the distinct folding process, verifying the decrease in defects by domain folding (Supplementary Fig. 11 and Supplementary Videos 1 and 2). On the basis of these results, microvoid defects are efficiently minimized by domain folding, from thick and long to thin and short, yielding less porosity in df-GFs.

Given the highly folded graphene sheets, smaller assembled graphene folds form in the df-GF, homogenizing and minimizing microvoids among folds. The representative df-GF sample has a high tensile strength of 5.19 GPa under chemical reduction at ambient condition of 25 °C, more than double the strength of ff-GF (2.32 GPa; Fig. 2j and Supplementary Fig. 12). In particular, the Young's modulus of df-GF reaches 529 GPa.

Relation of domain folding and mechanical properties

Delicate control of the domain-folded nanotexture was further achieved to investigate the relation of the assembled graphene folds, microvoids and mechanical properties (Fig. 3). The domain size (S, equal to D^2) for df-GF was modulated by adjusting the hole size (D^2: 144, 324 and 625 μm^2) of the microgrid, as shown in the cross-section of aerogel fibres (Fig. 2b,d and Supplementary Fig. 13). The length, thickness and area of the assembled graphene folds were statistically collected from the fibre cross-sections (Supplementary Fig. 14). Decreasing S gradually lessens the assembled graphene folds and narrows their size distribution. The assembled graphene folds of df-GF made from S of 144 μm^2 has an average length of 0.25 μm and an average thickness of 0.13 μm, 57.6% and 45.8% smaller than those (0.59 μm and 0.24 μm) of ff-GF, respectively. The corresponding fold area of df-GF was minimized by 77% (from 0.147 μm^2 to 0.034 μm^2) accompanied with a decreased coefficient of variation (CV) from 62.8% to 33.7%, compared with ff-GF fabricated from an intact spinneret domain (πr^2 = 5,024 μm^2, where r is the radius of spinneret; Fig. 3a). The tensile strength of GFs increases with the decrease in fold area (Fig. 3b). The df-GF fabricated from the finest fold area (0.034 μm^2) exhibits high strength of 5.19 ± 0.57 GPa, 153% higher than that (2.05 ± 0.31 GPa) of ff-GF. As the folds get both smaller and more uniform by decreasing the fold area, the cross-section of GF becomes smaller and more compact, and the physical density of GFs increases monotonically from 1.65 g cm^{-3} to 1.90 g cm^{-3}, corresponding to the optimization of porosity from 20.3% to 8.8% (Fig. 3c, Supplementary Fig. 15 and Supplementary Table 3).

https://doi.org/10.1038/s41563-025-02384-7

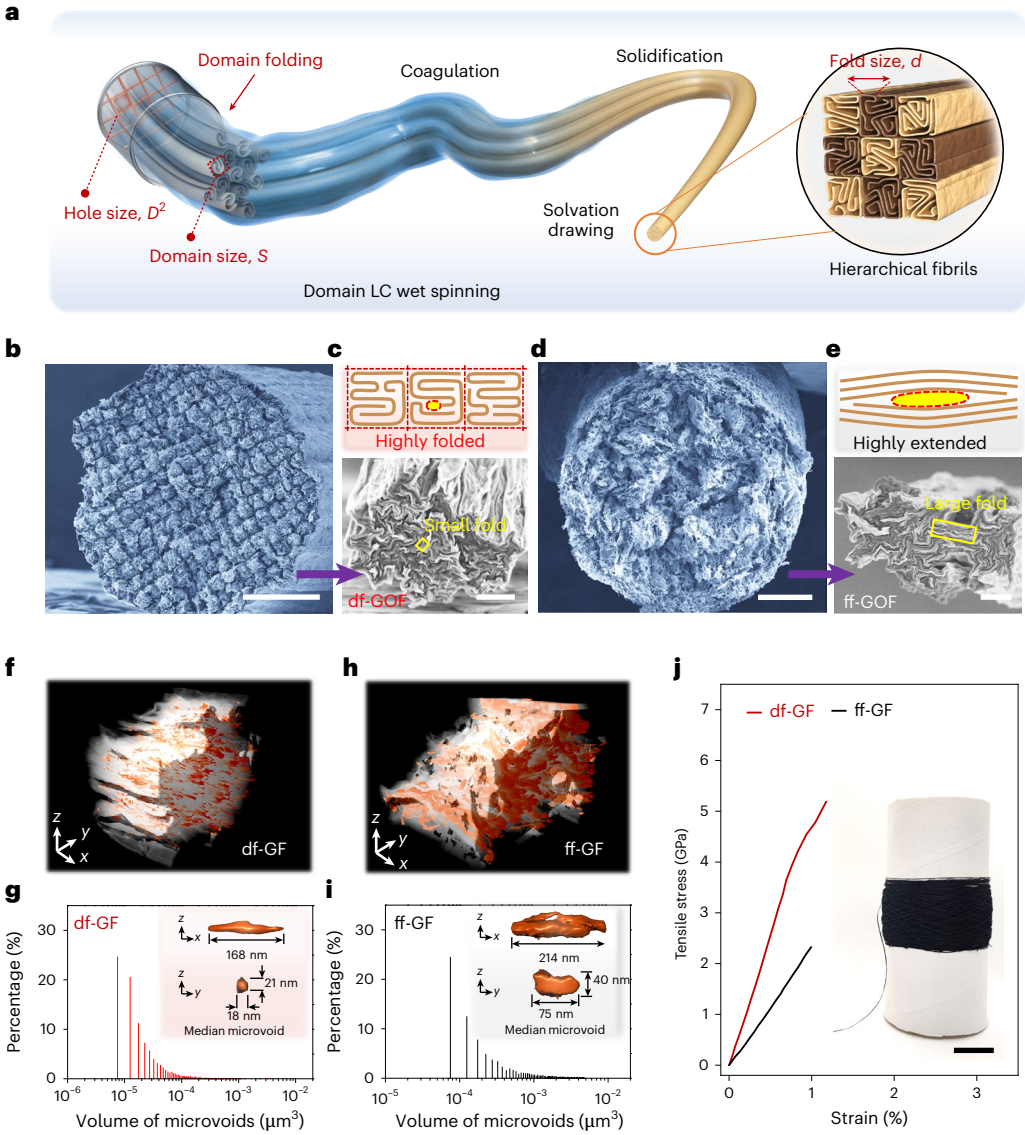

Fig. 2 | Preparation of df-GF. a, Schematic of the domain LC wet-spinning method, where hierarchically structured GOF composed of hundreds of interfused fibrils formed from highly folded graphene is fabricated by successive steps of domain folding, coagulation, solidification and solvation drawing. **b**–**e**, Structure schematics and SEM images of the aerogel fibre and coagulated solid fibre cross-sections of ff-GOF (**b** and **c**) and df-GOF (**d** and **e**), indicating the two models of highly folded (**c**) and highly extended sheets (**e**). Scale bars, 200 μm (**b** and **d**); 2 μm (**c** and **e**). **f**,**g**, 3D-reconstructed image (**f**) of microvoids derived from FIB-SEM tomography and volume distribution of microvoids (**g**) for df-GF. The insets show the microvoid at the median size within df-GF (**g**). **h**,**i**, 3D-reconstructed image (**h**) of microvoids derived from FIB-SEM tomography and volume distribution of microvoids (**i**) for ff-GF. The insets show the microvoid at the median size within the ff-GF (**i**). **j**, Typical tensile stress–strain curves of ff-GF and df-GF. The photograph in the inset shows the collected df-GFs after chemical reduction. Scale bar, 2 cm.

We further measured the size of the microvoids in GFs by small-angle X-ray scattering (SAXS) technology based on Ruland's streak method (Supplementary Fig. 16)[27,28]. As shown in Fig. 3d, as the fold area decreases, there is a sharp decrease by 66.4% in longitudinal length (L) of the microvoid from 154.3 nm to 51.9 nm, and by 23.5% from 3.02 nm to 2.31 nm for transverse width (l_p). The overall microvoid volume is decreased by 40% (Supplementary Fig. 17), in accordance with the tendency measured by physical density and 3D reconstruction. In particular, the misalignment angles (B_{eq}) are almost identically low, indicating that the ff-GF and three df-GFs have the same high orientation of microvoids with respect to the fibre axis. We also examined the porosity calculated from the invariant, demonstrating the coincidentally decreased microvoid volume with that from Ruland's method (Supplementary Fig. 18). Besides, the Porod slope was estimated to be 3.8, corresponding to a surface fractal microvoid structure with minor surface roughness (Supplementary Fig. 19)[29]. The high orientation of graphene sheets by effective solvation drawing is also necessary for high-performance GF (Supplementary Fig. 20 and Supplementary Table 4)[13,15,19,30,31]. Refining load-bearing units within materials could bear load uniformly and reducing the size of defects would hinder the initiating of critical cracks, thereby ensuring high mechanical strength[18,25,32]. Accordingly, the lessened assembled graphene folds and minimized microvoids (average volume from 1,101.9 nm^3 to 219.0 nm^3) originated from domain folding, facilitating a sharp increase in strength by 153% (Fig. 3e).

Strengthening mechanism

To further examine the strengthening mechanism, in situ Raman tests were used to investigate the stress distribution of fibres under tension. The downshift of the G-band denotes the strain of

https://doi.org/10.1038/s41563-025-02384-7

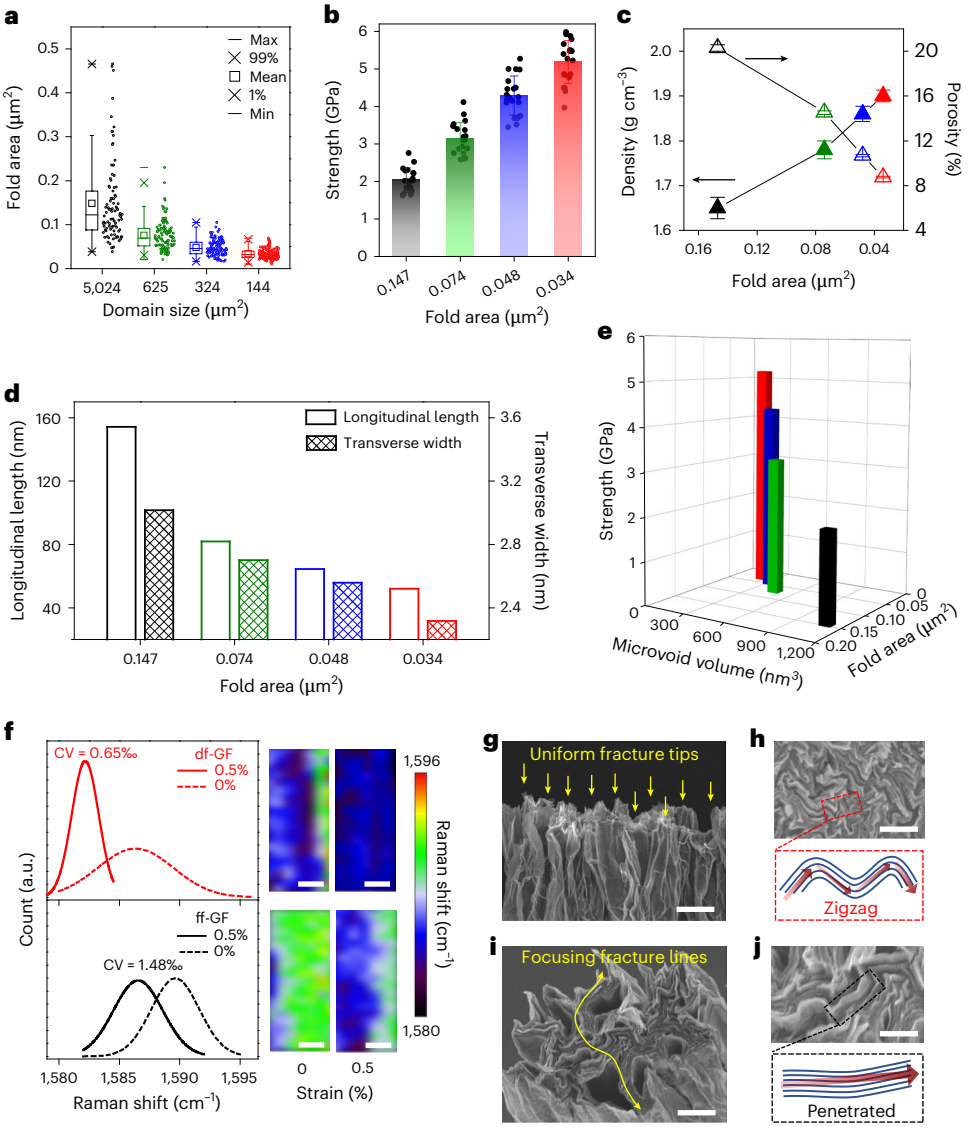

Fig. 3 | Characterization of GF structure and relationship with strength. **a**, Dependence of the assembled graphene fold area on the domain size of GFs. Data in **a** are represented as mean values ± one standard deviation for independent technical replicates ($n > 93$). **b**, Tensile strength of GFs made by different fold areas. Data in **b** are represented as mean values ± one standard deviation for independent technical replicates ($n = 20$). **c**,**d**, Dependence of the assembled graphene density and porosity on fold area (**c**) and microvoid size on fold area (**d**) of GFs. **e**, Relationship between the average tensile strength of GFs with microvoid volume and assembled graphene fold area. Note that SAXS could collect ultrasmall microvoids that cannot be observed by FIB-SEM tomography, thereby statistically obtaining a smaller average microvoid size. **f**, Raman shift distribution at 0.5% strain of df-GF and ff-GF (left) collected from mappings (right) of 5 × 10 μm². Scale bars, 2 μm. **g**–**j**, SEM images of fracture surfaces of df-GF (**g** and **h**) and ff-GF (**i** and **j**). Scale bars, 1 μm (**g** and **i**); 500 nm (**h** and **j**). The different fracture behaviours are illustrated in the dotted boxes. The df-GF mentioned above was made with the finest domain size (144 μm²).

graphene[33,34]. The G-band frequency distribution of df-GF (CV of 0.65 ‰) is 56% narrower than that (CV of 1.48 ‰) of ff-GF, at the same strain of 0.5% (Fig. 3f and Supplementary Fig. 21). The narrower distribution of the G-band at a given strain indicates the more uniform stress distribution in the high-strength df-GF[31], which results from small, uniform load-bearing units and minimized microvoids. The alleviated stress concentration of the fibre is further verified by the smaller range of stress distribution in the coarse-grained molecular dynamics simulations (Supplementary Fig. 22). GFs from the folding process of two-dimensional graphene have distinct microvoids ('through cracks' between the graphene layers) from conventional fibres from 1D chains/nanotubes. These through cracks are more detrimental for the fibre strength due to the higher stress concentration factor, implying the notable importance in controlling the microvoids of GFs (Supplementary Fig. 23c). We delicately controlled the domain-folded nanotexture and minimized microvoids in GFs, resulting in the more uniform stress distribution and high strength of df-GF.

A more effective load transfer was also proven by the higher G-band shift rate as measured during real-time tensile testing (8.8 cm^{-1} compared with 5.1 cm^{-1} per 1% strain; Supplementary Fig. 24). Decreased content of microvoids (that is, increased density) benefits the load-bearing volume (Supplementary Fig. 23)[26]. Furthermore, the sheet alignment of df-GF is improved with an average Herman's order of 0.94 (removing the isotropic background and using a Gaussian fit, in both SAXS and wide-angle X-ray scattering (WAXS) results). Thus, the increased load transfer in df-GF comes from the more effective interaction among interlocked and aligned sheets with minimized content of microvoids, which greatly promotes the Young's modulus of fibres (Supplementary Figs. 25 and 26).

https://doi.org/10.1038/s41563-025-02384-7

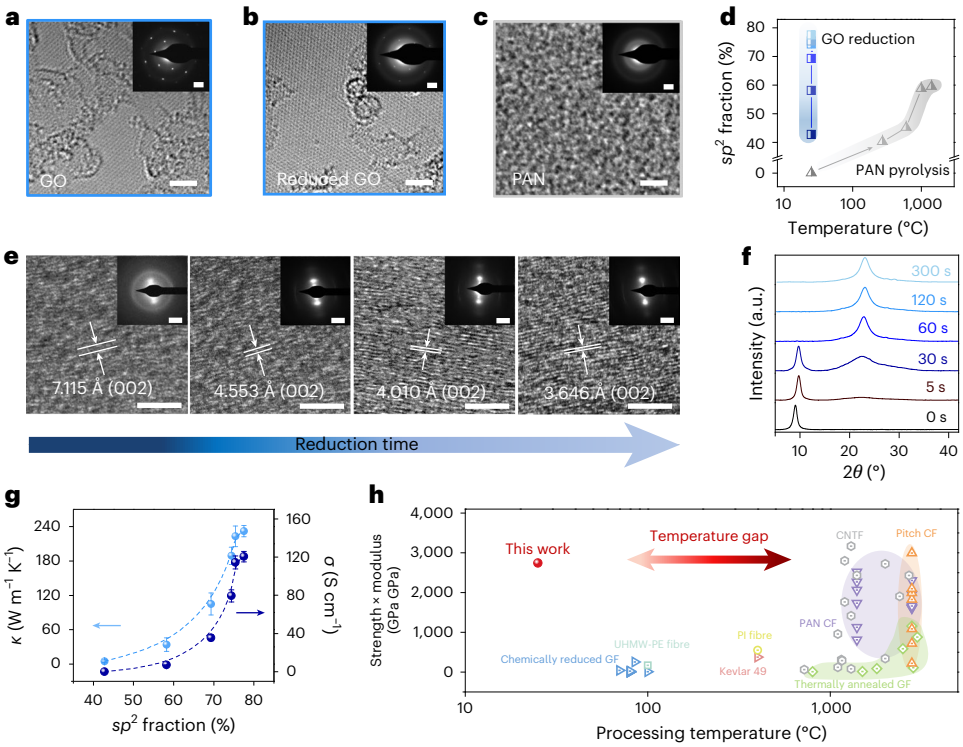

Fig. 4 | Structural evolution and property relationships of GF. a–**c**, TEM images of the atomic structure of monolayer GO sheet (**a**), monolayer reduced GO sheet (**b**) and pristine PAN (**c**). Scale bars, 2 nm. The insets show the corresponding SAED patterns. Scale bars, 3 nm^{-1}. **d**, sp^2 fractions of fibres in two paths tracked by X-ray photoelectron spectroscopy. **e**,**f**, Structure evolution from GOF to GF tracked by TEM (**e**) and XRD (**f**). Scale bars, 5 nm (**e**). The insets show the corresponding SAED patterns. Scale bars, 3 nm^{-1}. **g**, Relationships of structural evolution on thermal and electrical conductivities. Data are represented as mean values ± one standard deviation for independent technical replicates ($n = 3$). **h**, Ashby chart of strength × modulus versus processing temperature, illustrating a general rule that higher mechanical properties of fibre materials are achieved by increasing the input energy. Our fibres break the critical rule and achieve high strength and modulus at room temperature.

The fracture surface and section were also detected. The df-GF shows jagged fracture tips (Fig. 3g), indicating stress concentration relief, crack deflection and zigzag crack propagation through highly folded graphene sheets (Fig. 3h)[35]. Conversely, the flat fracture surface evidences catastrophic rupture by serious stress concentration, leading to penetrated cracks through highly extended sheets in the cross-section of ff-GFs (Fig. 3i,j).

Graphene units ensuring room-temperature high-performance CFs

The structural graphene nature of GO allows preparing CFs with qualified carbon content and performances through efficient reduction at room temperature. Although being oxidized, the monolayer GO sheet maintains the integration of graphene backbone, as proved by the hexagonal sharp spots of its selected area electron diffraction (SAED) pattern[36] (Fig. 4a). After room-temperature reduction, sp^2-hybridized carbon zones become continuous and the graphene backbones are restored to show sharper SAED spots (Fig. 4b). Tracked by Raman spectra, the efficiency of the chemical reduction of the GO sheet was proved by the increased intensity ratio of D and G bands (I_D/I_G) within 60 s (Supplementary Fig. 27). The increased I_D/I_G indicates the enlarged mean distance between defects due to the restored sp^2 graphene domains[37].

Room-temperature reduction of GO laminates generates highly crystalline graphitic units, which are the essential structural units for high-performance CFs. The highly crystalline graphitic units are composed of ordered graphene sheets, showing a closer crystalline structure to high-modulus pitch CFs at a scale of hundreds of nanometres[1], besides the domain-folded interlocked graphene folds at a larger scale. We revealed that the crystallinity of GF after room-temperature reduction is even higher than the counterpart of PAN CF processed above 1,300 °C. The interlayer spacing of GF quickly decreased to 3.646 Å within 300 s of reduction, as tracked by transmission electron microscopy (TEM; Fig. 4e) and X-ray diffraction (XRD; Fig. 4f). On the contrary, the fibre derived from the organic PAN precursor (Fig. 4c) processed above 1,300 °C has a lower crystallinity with turbostratic carbons and a larger interlayer spacing of 3.698 Å (Supplementary Fig. 28). PAN and pitch CFs require high-temperature heat treatment (2,700 °C for PAN and 2,000 °C for pitch) to attain high graphitic crystallinity[38,39]. Evaluating the overall chemical composition by X-ray photoelectron spectroscopy, the carbon content of GF rises from 72.1% to a high level of 92.3%, approaching that of PAN annealed at around 1,000 °C. The sp^2-hybridized carbon of GF is restored from 42.8% to 77.5%, which is 30% higher than that (59.5%) of PAN CF annealed at 1,300 °C (Fig. 4d, Supplementary Figs. 29 and 30 and Supplementary Table 5). The restoration of the sp^2 structure leads to decreased interlayer space, thereby enforcing the interlayer interaction by 735% than the GO precursor, as proved by density functional theory calculations (Supplementary Fig. 31). The growth of the conductive area was depicted by conductive atomic force microscopy (CAFM; Supplementary Fig. 32). The non-continuous π-conjugated regions (bright regions in CAFM images) and partially restored sp^2 graphene domains limit the electrical conductivity (120 S cm^{-1}) compared with the high conductivity of carbon nanotube fibres and thermally annealed GFs (Supplementary Table 6)[15,17,18,40,41]. However, the electrical conductivity of room-temperature df-GF is comparative with that of traditional CFs carbonized under 800–900 °C. Given the highly crystalline and ordered graphene structures (Supplementary Fig. 33), df-GF has a high thermal conductivity (232 W m^{-1} K^{-1}) achieved under room temperature (Fig. 4g, Supplementary Fig. 34 and Supplementary Table 7).

GFs annealed at high temperature usually have better strength and Young's modulus than those processed at lower temperature, because restored atomic defects (from GO to graphene) and more crystalline structure lead to decreased interlayer spacing and stronger interaction (Supplementary Figs. 31 and 35)[42]. We demonstrated that minimizing the assembly defects in GFs significantly improved the mechanical properties even without fully restoring the perfect graphene lattice by thermal treatment. The df-GFs prepared by minimizing assembly defects takes the extreme corner of high strength, high modulus and room-temperature preparation, which is a forbidden mission in the path of organic carbonization. (Fig. 4h). The large temperature gaps between GF and other carbonaceous fibres highlight the energy-saving superiority of preparing high-performance CFs at room temperature along the graphene assembly path. Compared with previously reported chemically reduced GFs at 50–90 °C and thermally annealed GFs above 1,000 °C, this work achieved high performances by the philosophy of domain-folded nanotexture to make df-GF as a competitive candidate of room-temperature high-performance CFs (Supplementary Fig. 35). For all kinds of reported fibre, a high modulus (>400 GPa) is only achieved by high-temperature treatment. Trading off high strength and high modulus under room temperature is a big challenge. We further define a factor $f = \sigma M/E_c$ to display the efficiency of mechanical property to energy consumption, where σ is the tensile strength, M is Young's modulus and E_c is the energy consumption. The room-temperature-prepared df-GF shows an enhanced factor f, simultaneously achieving high strength and high modulus. This breakthrough surpasses the existing mechano-energy limit of thermally carbonized and graphitized GFs, CFs, carbon nanotube fibres, inorganic fibres and polymer fibres, providing valuable insights for the development of high-performance fibres (Supplementary Figs. 35 and 36 and Supplementary Table 8). In particular, stable values of mechanical strength were measured under a short gauge length of 5 mm (CV of 11%). Decreased and widely distributed mechanical strength (average of 3.83 GPa with CV of 38%) under a longer gauge length of 25 mm indicates the chance occurrence of a defect within the gauge length (Supplementary Fig. 37), which is often recognized at an early stage in the development of any commercial fibre[43].

We also demonstrate the generality of the domain-folding strategy by strengthening other two-dimensional nanosheet assembled fibres and graphene-based composite fibres (Supplementary Fig. 38 and Supplementary Table 9). MXene aerogel fibres also display a domain-folded cross-section like that of GO and the tensile strength of domain-folded MXene fibre is enhanced by 82.5% compared with that of free-folded MXene fibre (Supplementary Fig. 39a,b). Moreover, domain LC forms in the composite solution of GO and even at lower GO content of 20 wt% (Supplementary Fig. 40). A small amount of GO acts as the dominant seed to control the assembly behaviour of domain folding, thereby strengthening the composite fibre (Supplementary Fig. 39c–g). The tensile strength of domain-folded GO/PAN composite fibre with GO loading of 30 wt% is enhanced by 45.8% compared with the free-folded fibre (Supplementary Fig. 39h).

In conclusion, we proposed the room-temperature preparation of CFs with high mechanical performances and excellent functionalities from GO precursor. The graphene assembly path could become an inspiring paradigm for CF production. The precise control of the domain-folded nanotexture minimizes assembly defects and makes the fibre strong and stiff. We foresee that the room-temperature preparation of GFs will inspire the traditional CF production process.

Online content

Any methods, additional references, Nature Portfolio reporting summaries, source data, extended data, supplementary information, acknowledgements, peer review information; details of author contributions and competing interests; and statements of data and code availability are available at https://doi.org/10.1038/s41563-025-02384-7.

References

1. Frank, E., Steudle, L. M., Ingildeev, D., Spörl, J. M. & Buchmeiser, M. R. Carbon fibers: precursor systems, processing, structure, and properties. *Angew. Chem. Int. Ed.* **53**, 5262–5298 (2014).
2. Moreton, R., Watt, W. & Johnson, W. Carbon fibres of high strength and high breaking strain. *Nature* **213**, 690–691 (1967).
3. Anguita, J. V. et al. Dimensionally and environmentally ultra-stable polymer composites reinforced with carbon fibres. *Nat. Mater.* **19**, 317–322 (2020).
4. Chae, H. G. et al. High strength and high modulus carbon fibers. *Carbon* **93**, 81–87 (2015).
5. Chen, S., Qiu, L. & Cheng, H. M. Carbon-based fibers for advanced electrochemical energy storage devices. *Chem. Rev.* **120**, 2811–2878 (2020).
6. Badami, D. V., Joiner, J. C. & Jones, G. A. Microstructure of high strength, high modulus carbon fibres. *Nature* **215**, 386–387 (1967).
7. Diefendorf, R. J. & Tokarsky, E. High-performance carbon fibers. *Polym. Eng. Sci.* **15**, 150–159 (1975).
8. Zhang, W., Liu, J. & Wu, G. Evolution of structure and properties of PAN precursors during their conversion to carbon fibers. *Carbon* **41**, 2805–2812 (2003).
9. Ashby, M. F. *Materials Selection in Mechanical Design* (Elsevier, 2011).
10. Choi, D., Kil, H. S. & Lee, S. Fabrication of low-cost carbon fibers using economical precursors and advanced processing technologies. *Carbon* **142**, 610–649 (2019).
11. Xu, Z. & Gao, C. Graphene chiral liquid crystals and macroscopic assembled fibres. *Nat. Commun.* **2**, 571 (2011).
12. Xin, G. et al. Highly thermally conductive and mechanically strong graphene fibers. *Science* **349**, 1083–1087 (2015).
13. Xu, Z. et al. Ultrastiff and strong graphene fibers via full-scale synergetic defect engineering. *Adv. Mater.* **28**, 6449–6456 (2016).
14. Xin, G. et al. Microfluidics-enabled orientation and microstructure control of macroscopic graphene fibres. *Nat. Nanotechnol.* **14**, 168–175 (2019).
15. Li, P. et al. Highly crystalline graphene fibers with superior strength and conductivities by plasticization spinning. *Adv. Funct. Mater.* **30**, 2006584 (2020).
16. Wang, Y. et al. Determinative scrolling and folding of membranes through shrinking channels. *Sci. Adv.* **10**, eadm7737 (2024).
17. Lee, D. et al. Ultrahigh strength, modulus, and conductivity of graphitic fibers by macromolecular coalescence. *Sci. Adv.* **8**, eabn0939 (2022).
18. Zhang, X. et al. Carbon nanotube fibers with dynamic strength up to 14 GPa. *Science* **384**, 1318–1323 (2024).
19. Ding, L. et al. Covalently bridging graphene edges for improving mechanical and electrical properties of fibers. *Nat. Commun.* **15**, 4880 (2024).
20. Xu, Z., Sun, H., Zhao, X. & Gao, C. Ultrastrong fibers assembled from giant graphene oxide sheets. *Adv. Mater.* **25**, 188–193 (2013).
21. Chang, D. et al. Reversible fusion and fission of graphene oxide-based fibers. *Science* **372**, 614–617 (2021).
22. Jiang, Y., Guo, F., Xu, Z., Gao, W. & Gao, C. Artificial colloidal liquid metacrystals by shearing microlithography. *Nat. Commun.* **10**, 4111 (2019).
23. Jensen, F. Activation energies and the Arrhenius equation. *Qual. Reliab. Eng. Int.* **1**, 13–17 (1985).
24. Wegst, U. G. K., Bai, H., Saiz, E., Tomsia, A. P. & Ritchie, R. O. Bioinspired structural materials. *Nat. Mater.* **14**, 23–36 (2015).
25. Whitney, W. & Kimmel, R. M. Griffith equation and carbon fibre strength. *Nat. Phys. Sci.* **237**, 93–94 (1972).
26. Pan, H. H. & Weng, G. J. Elastic moduli of heterogeneous solids with ellipsoidal inclusions and elliptic cracks. *Acta Mech.* **110**, 73–94 (1995).

27. Zhu, C. et al. A small-angle X-ray scattering study and molecular dynamics simulation of microvoid evolution during the tensile deformation of carbon fibers. *Carbon* **50**, 235–243 (2012).
28. Thünemann, A. F. & Ruland, W. Microvoids in polyacrylonitrile fibers: a small-angle X-ray scattering study. *Macromolecules* **33**, 1848–1852 (2000).
29. Yue, H. et al. Fractal carbon nanotube fibers with mesoporous crystalline structure. *Carbon* **122**, 47–53 (2017).
30. Bai, Y. et al. Carbon nanotube bundles with tensile strength over 80 GPa. *Nat. Nanotechnol.* **13**, 589–595 (2018).
31. Li, P. et al. Continuous crystalline graphene papers with gigapascal strength by intercalation modulated plasticization. *Nat. Commun.* **11**, 2645 (2020).
32. Bennett, S. C., Johnson, D. J. & Johnson, W. Strength-structure relationships in PAN-based carbon fibres. *J. Mater. Sci.* **18**, 3337–3347 (1983).
33. Huang, Y. & Young, R. J. Effect of fibre microstructure upon the modulus of PAN- and pitch-based carbon fibres. *Carbon* **33**, 97–107 (1995).
34. Frank, O. et al. Development of a universal stress sensor for graphene and carbon fibres. *Nat. Commun.* **2**, 255 (2011).
35. Bouville, F. et al. Strong, tough and stiff bioinspired ceramics from brittle constituents. *Nat. Mater.* **13**, 508–514 (2014).
36. Huang, M. et al. Large-area single-crystal AB-bilayer and ABA-trilayer graphene grown on a Cu/Ni(111) foil. *Nat. Nanotechnol.* **15**, 289–295 (2020).
37. Cançado, L. G. et al. Quantifying defects in graphene via Raman spectroscopy at different excitation energies. *Nano Lett.* **11**, 3190–3196 (2011).
38. Fitzer, E. PAN-based carbon fibers. Present state and trend of the technology from the viewpoint of possibilities and limits to influence and to control the fiber properties by the process parameters. *Carbon* **27**, 621–645 (1989).
39. Qin, X., Lu, Y., Xiao, H., Wen, Y. & Yu, T. A comparison of the effect of graphitization on microstructures and properties of polyacrylonitrile and mesophase pitch-based carbon fibers. *Carbon* **50**, 4459–4469 (2012).
40. Li, P. et al. Bidirectionally promoting assembly order for ultrastiff and highly thermally conductive graphene fibres. *Nat. Commun.* **15**, 409 (2024).
41. Newcomb, B. A. Processing, structure, and properties of carbon fibers. *Compos. Part A* **91**, 262–282 (2016).
42. Pugno, N. M. The design of self-collapsed super-strong nanotube bundles. *J. Mech. Phys. Solids* **58**, 1397–1410 (2010).
43. Koziol, K. et al. High-performance carbon nanotube fiber. *Science* **318**, 1892–1895 (2007).

Methods

Materials

Aqueous GO dispersions (average size, 101 μm) were purchased from Hangzhou Gaoxi Technology (www.gaoxitech.com). Other reagents were purchased from Sinopharm Chemical Reagent and used as received.

Preparation of spinning dope

GO spinning dope: spinning dope of GO in N,N-dimethyl formamide (DMF) was obtained by replacing water in an aqueous GO solution via repeated centrifugation. GO DMF spinning dope was used to continuously fabricate GFs.

GO/PAN spinning dope: PAN powders were dissolved in DMF forming a solution with a mass fraction of 1 wt%. The concentration of GO DMF solution was also adjusted to be 1 wt%. To prepare the GO/PAN spinning dope with different mass fractions, the GO and PAN solutions were mixed by volume, denoted as 0GO-100PAN, 10GO-90PAN, 20GO-80PAN, 30GO-70PAN, 50GO-50PAN and 100GO-0PAN (Supplementary Fig. 39).

MXene spinning dope: the MXene aqueous dispersion was concentrated to 20 mg g^{-1} as a spinnable dope.

Fabrication of df-GF and ff-GF

First, the spinning dope was carefully filtered to remove possible impurities that may plug the microgrid. Second, degassed GO spinning dope was forced to pass through the microgrid and extruded into the coagulation bath (ethyl acetate). Different microgrids (D^2: 144, 324 and 625 μm^2) were used to prepare df-GF. Then, the nascent fibre was continuously drawn in a solvation-drawing bath (1:5 ratio of water and acetic acid) to produce GOF with a drawing ratio of up to 60%. Finally, df-GF was obtained after reduction in an efficient reduction bath (1:6 ratio of hydriodic acid and trifluoroacetic acid) and washing with ethanol. The ff-GF was prepared along the same way (diameter of spinneret, 80 μm) as df-GF without the microgrid in the spinneret and solvation drawing in water and acetic acid.

Fabrication of the MXene fibres and aerogel fibres

The coagulation bath was made by a 1:1 mixture of 10 wt% of NH_4Cl aqueous solution and 4 vol% of NH_4OH aqueous solution according to previous reports[44]. The MXene aqueous dope was extruded through the microgrid (D = 40 μm) into the coagulation bath. Then, the coagulation bath was replaced by deionized water. Directly drying the gel fibre produced the domain-folded MXene fibre and freeze drying the gel fibre obtained the corresponding aerogel fibre. The control sample of the free-folded MXene fibre was fabricated without the embedded microgrid.

Fabrication of PAN/GO composite fibres and aerogel fibres

The spinning dope was extruded through the microgrid (D = 40 μm) into a coagulation bath of EA and continuously collected as domain-folded GO/PAN composite fibres. The control sample of free-folded GO/PAN composite fibres was fabricated without the embedded microgrid. To prepare the aerogel fibre, the dope was extruded into a coagulation bath of $CaCl_2$ solution (3 wt%) and then the gel fibre was washed with deionized water and finally freeze dried.

Mechanical tests of fibre

Stress–strain curves of the fibres were obtained by testing the fibres at a gauge length of 5 mm for stable measurement with a nanomechanical tester of Keysight T150 UTM (maximum load, 500 mN; load resolution, 50 nN) at a tensile rate of $1.67 \times 10^{-2}\,s^{-1}$. Measuring at a larger gauge length of 25 mm leads to a larger CV of 38%, which is often observed at an early stage in the development of any commercial fibre and is in accordance with previous literature[43]. The tensile stress was obtained by dividing the load by the cross-sectional area of the fibre. Each fractured sample was collected, and the cross-section was observed by SEM, followed by measuring the cross-sectional area. The strain was obtained by dividing the measured displacement by the initial gauge length. Compressive strength was measured to be 811 MPa by tensile recoil tests[45].

Instruments and characterization

The aerogel fibres were fabricated by freeze drying and used for comparison of GO distribution of df-GF and ff-GF with field-emission SEM (Hitachi S4800). The SAXS experiments were carried out at the beamline BL10U1 and BL16B1 at Shanghai Synchrotron Radiation Facility, with a sample-to-detector distance of 4,500 mm and 2,000 mm, to characterize the microvoid structure and orientation, respectively. The WAXS experiments were carried out at the beamline BL16B1 at the Shanghai Synchrotron Radiation Facility with a sample-to-detector distance of 72 mm, to determine the alignment of graphene sheets. These patterns were background subtracted to remove the isotropic contribution. Both SAXS and WAXS tests were conducted using a bundle of fibres under X-ray exposure.

In situ Raman test was operated by Renishaw inVia Reflex Raman microscopy (excitation wavelength, 532 nm) accompanied with a translation stage (PI, M-112.2DG1) with an accuracy of 250 nm. The spinneret channel was characterized by microcomputed tomography (Carl Zeiss, 520 Versa). The serial sections of df-GF and ff-GF were obtained by FIB-SEM tomography (Helios G3 UC) with a constant separation of 10 nm.

The assembled graphene fold sizes for different fibres were collected by cross-sections of more than five specimens observed by SEM. The fibre density was tested by the sink–float method, in which three types of liquid—tetrabromoethane, carbon tetrachloride and hexamethylene—were used to obtain different densities, and the fibre porosity was calculated by the density and XRD interlayer spacing[12,39]. The linear density of a fibre was measured by weighing the kilometres long fibre using an electronic microbalance (QUINTIX35-1CN; accuracy, 0.01 mg). FIB (Helios 450HP) was used to prepare the axial slices. The sliced samples were characterized by TEM (FEI Tecnai, G2) operated at 300 kV. Monolayer reduced GO was obtained by reducing the monolayer GO deposited on a gold grid immersing in the same reduction bath as used in GF for different times. These monolayer samples were characterized by TEM operated at 80 kV. The electrical conductivity was measured by a standard four-probe method on an electrical transport properties measurement system comprising a Keithley 2460 source meter. The thermal conductivity of the GF was measured by a well-established T-type method[46].

The compositions of GFs were measured by X-ray photoelectron spectroscopy (ESCALAB 250Xi) and all the binding energies were referenced to the C1*s* neutral carbon peak at 284.8 eV. The interlayer spacing was measured by XRD (PANalytical X'Pert3 Powder-17005730) using monochromatic Cu Kα radiation (wavelength, 0.154 nm).

CAFM analyses were conducted with a Cypher-S (Asylum Research) atomic force microscope in the contact mode located in a glovebox filled with nitrogen. Smooth reduced GO films, prepared in the same reduction bath as GF but with varying reduction times, were analysed by CAFM.

Characterization of the microvoid structure

The parameters of microvoids in GFs could be calculated according to Ruland's streak method[27,28]:

$$s^2 B^2_{\pi/2}(s) = \frac{1}{L^2} + s^2 B_{eq}, \quad (1)$$

where $B_{\pi/2}(s)$ is the integration breadth along azimuthal scan, L is the length of the microvoids and B_{eq} is the orientation angle of the microvoids. The values of L and B_{eq} can be obtained from the intercept and

slope of the $s^2B^2_{\pi/2}(s)$–s^2 plot in equation (1). The experimental data and their fitting results are shown in Supplementary Fig. 16.

Inserting the values of L and B_{eq}, the number of microvoids n and the average chord length in the cross-section of microvoids l_p can be obtained via equations (2) and (3) by fitting the theoretical to experimental $I(s, \pi/2)$–s curve.

$$I(s,\pi/2) \propto n\rho_m^2 \frac{L^2}{\sqrt{1+(sLB_{eq})^2}} |\Phi_D|^2(s), \quad (2)$$

where

$$|\Phi_D|^2(s) \propto \frac{l_p^4}{\left[1+(2\pi l_p s)^2\right]^3}. \quad (3)$$

The relative volume of microvoids V_{rel} can be evaluated approximately by $V \approx nLl_p^2$. V_{rel} is the ratio of the microvoids volume content in the samples to the precursor fibres.

The average microvoid volume in GFs could be approximately calculated as cylinder by $V_0 = \frac{\pi}{4} l_p^2 L$.

Calculation of orientation

The orientation order was quantified by converting the orientation distribution into Herman's orientation function f defined as[31,47]

$$f = \left\langle \frac{3}{2}\cos^2\varphi - \frac{1}{2} \right\rangle, \quad (4)$$

where φ is the azimuthal distribution and $\cos^2\varphi$ is the average value of the square of the cosine of angle φ. Assuming rotational symmetry of the fibre axis, the following equation is obtained.

$$\cos^2\varphi = \frac{\int_0^{\frac{\pi}{2}} I(\varphi)\cos^2\varphi \sin\varphi \mathrm{d}\varphi}{\int_0^{\frac{\pi}{2}} I(\varphi)\sin\varphi \mathrm{d}\varphi}, \quad (5)$$

where $I(\varphi)$ is the intensity at φ in the azimuthal scanning curve.

Data availability

The data that support the findings of this study are available in the Article and the Supplementary Information. Source data are provided with this paper.

References

44. Eom, W. et al. Large-scale wet-spinning of highly electroconductive MXene fibers. *Nat. Commun.* **11**, 2825 (2020).
45. Allen, S. R. Tensile recoil measurement of compressive strength for polymeric high performance fibres. *J. Mater. Sci.* **22**, 853–859 (1987).
46. Ma, W. et al. Systematic characterization of transport and thermoelectric properties of a macroscopic graphene fiber. *Nano Res.* **9**, 3536–3546 (2016).
47. Wan, S. et al. High-strength scalable graphene sheets by freezing stretch-induced alignment. *Nat. Mater.* **20**, 624–631 (2021).

Acknowledgements

We thank the staff members at the Shanghai Synchrotron Radiation Facility for assistance in WAXS and SAXS characterizations, J. Guo in the Centre of Cryo-Electron Microscopy (CCEM), Zhejiang University, for his technical assistance on 3D construction of GF by SEM-FIB tomography, and Z. Lin and W. Ma in the Department of Engineering Mechanics, Tsinghua University, for their help on the measurement of thermal conductivity. This work is supported by the National Natural Science Foundation of China (52090031, 52090030, 52403051 and 52272046) (C.G., P.L. and Y.L.), Natural Science Foundation of Zhejiang Province (LQN25E030008 and LR23E020003) (P.L. and Y.L.), National Key Research and Development Program of China grants (2022YFA1205300 and 2022YFA1205301) (Zhen Xu), 'Pioneer' and 'Leading Goose' R&D Program of Zhejiang grant (2023C01190) (Zhen Xu), Fundamental Research Funds for the Central Universities grant (226-2024-00074) (Zhen Xu), Shanxi-Zheda Institute of New Materials and Chemical Engineering (2022SZ-TD011 and 2022SZ-TD012) (C.G. and Zhen Xu) and the International Research Centre for X polymers.

Author contributions

P.L., Zhen Xu and C.G. contributed to the initiating idea. Z.W. and P.L. performed the experiments. Z.W. and G.C. contributed to the preparation of fibres and mechanical tests. Y.Z. and Zhiping Xu contributed to the theoretical analysis of the activation energy of chemical reduction and stress distribution of fibres. Z.L. contributed to the theoretical analysis of interaction of graphene. Z.D., X.M. and B.W. helped to prepare the fibres. Y.L. and W.G. participated in the discussion of strengthening strategy. P.L., Z.W., Zhen Xu and C.G. analysed all the data and wrote the manuscript. All authors commented on the manuscript.

Competing interests

The authors declare no competing interests.

Additional information

Supplementary information The online version contains supplementary material available at https://doi.org/10.1038/s41563-025-02384-7.

Correspondence and requests for materials should be addressed to Zhen Xu, Zhiping Xu, Yingjun Liu or Chao Gao.

Peer review information *Nature Materials* thanks Kelvin Fu and the other, anonymous reviewer(s) for their contribution to the peer review of this work.